communications materials

A Nature Portfolio journal

Article

https://doi.org/10.1038/s43246-026-01096-y

Defect-assisted refinement of nanoscale alpha in titanium alloys

Abigail K. Ackerman[1], Benjamin H. Savitzky[2], Colin Ophus[3,4], Mohsen Danaie[5], Phani Karamched[6] & David Dye[1]

Titanium alloys owe their superior fatigue performance to a lack of extrinsic nucleation sites for cracking, but this also results in difficulty in developing fine, 10 nm scale precipitates to provide fatigue strength. Conventional Ti alloys used for large components such as jet engine discs must instead develop a hierarchical microstructure through successive waves of nucleation. Here we show that intermediate temperature deformation can result in the nucleation of nanoscale hcp α precipitates in between large μm thick α plates, and observe the precipitation of these in situ in the TEM using 4D-Scanning Transmission Electron Microscopy (4D-STEM) alongside the accompanying partially-relaxed transformation strain fields. This results in an improvement in the high cycle fatigue strength of the material by 95 MPa, to around 920 MPa in un-notched high cycle fatigue at 10^6 cycles, or 200 MJ kg^{-1}, which is among the highest of all structural materials.

Titanium alloys are essential for critical rotating parts in jet engines because of their unsurpassed fatigue-allowable specific strengths[1,2]. This is due to both the low density (4.5 g cm^{-3}) and the lack of extrinsic defects such as the inclusions found in super-clean steels and nickel-based superalloys. The ability of liquid titanium to dissolve its own oxide enables defect-free microstructures when wrought processing methods are employed, particularly when ceramic casting moulds are avoided[3,4]. This defect free wrought microstructure means that the fatigue initiating feature within the material can be microstructural in origin. Furthermore, titanium alloys retain their strength at elevated temperatures, with near-α alloys performing reliably up to approximately 570 °C. Beyond this limit, their temperature capability is constrained by burn resistance, driven by runaway exothermic oxidation. A defining feature of titanium alloys is their solid-state phase transformation, which can be harnessed to engineer fine-scale microstructures through length-scale strengthening mechanisms. However, the formation of the low-temperature hexagonally close-packed (*hcp*) α phase is typically restricted to nucleation sites at grain boundaries of the high-temperature body-centred cubic (*bcc*) β phase or from pre-existing α precipitates[5–7]. This limits the potential for microstructural refinement, presenting a critical challenge in the development of next-generation titanium alloys.

Structural materials are strengthened by inhibiting the motion of dislocations using grain and phase boundaries, as well as harnessing the intrinsic strength of the dislocations themselves. Consequently the design of tough, high strength alloys requires the strengthening of boundaries across the lengthscales, from nm to μm. Microstructure engineering of titanium alloys exploits the solid-state transformation between the high temperature β phase and the low temperature α phase, enabling a balance of strength and ductility.

Ti-6Al-2Sn-4Zr-6Mo is a prototypical high strength titanium alloy widely used in jet engine compressor components, distinguished by its exceptional high cycle fatigue resistance (825 MPa at 1×10^6 un-notched cyclic life, and an ultimate tensile strength of 1170 MPa[8,9]). Its superior mechanical performance arises from a hierarchical microstructure, with 1 μm wide basketweave primary α plates that nucleate from prior β grain boundaries. Lengthscale strengthening is then further provided by finer secondary α precipitates, 20–100 nm wide, grown at a lower temperature, which nucleate from the primary α_p[10]. However, these secondary α precipitates inherit their crystallographic orientation from the parent primary α plates, with limited variation on side-branching, thereby constraining the extent of microstructural refinement[11,12].

However, there have been hints in the literature that suggest in heavily β-stabilised alloys with very slow α growth kinetics, such as Ti-5553, dislocations may serve as heterogeneous nucleation sites for α precipitates, yielding exceptionally fine secondary α features (~ 20 nm). Recently studies report that in very highly β stabilised titanium alloys, prior deformation can provide a dislocation content that can act as sources for α nucleation[13,14]. In addition, cold worked thin sheet Ti alloys such as β-21S can develop very high strengths on subsequent ageing[15]. Despite these advances, controlled

---

[1]Department of Materials, Royal School of Mines, Imperial College London, London, UK. [2]NCEM, Lawrence Berkeley National Laboratory, University of California, Berkeley, CA, USA. [3]Department of Materials Science and Engineering, Stanford University, Stanford, CA, USA. [4]Precourt Institute for Energy, Stanford University, Stanford, CA, USA. [5]Electron Physical Sciences Imaging Centre (ePSIC), Diamond Light Source, Didcot, UK. [6]Department of Materials, University of Oxford, Oxford, UK. e-mail: a.ackerman14@imperial.ac.uk

strategies to produce such nanoscale secondary α have not been developed for widely used α+β alloys such as Ti-6246 and Ti-6Al-4V (Ti-64).

Here, we demonstrate that cold and warm working can be used to induce a dislocation content that results in the precipitation of fine scale secondary α, avoiding conventional nucleation from the adjacent primary α plates, and observe this process in situ. We also measure the elastic strains around such plates using nanobeam electron diffraction (NBED), and analyse the resulting effect of secondary α orientation. We have further verified that the resulting microstructure results in superior fatigue behaviour as well as conventional tensile performance.

Results

Characterisation

The results from the as-received, cold rolled and aged and warm rolled and aged samples can be seen in Fig. 1. Imaging using scanning electron microscopy was completed using backscatter electron (BSE) mode, which is dependent on the Z number of the elements present in the sample and therefore highlights the microstructure in these samples due to elemental partitioning to the different phases present. The as-received microstructure has large primary α grains indicated on the figure, and smaller secondary α laths, appearing as a dark grey elongated morphology, within a light grey β matrix. The cold rolled and aged and the warm rolled and aged samples show significantly finer secondary α within the β matrix. The size of the primary α is consistent between all specimens as shown in Fig. 1, with a lath width of roughly ~ 1 μm showing that the size change in the secondary α is a direct result of the rolling and ageing. Additionally, any further mechanical testing results should be directly dependent on the size change of the secondary α due to the consistency of the primary α laths observed. The secondary α lath width reduced from ~ 50–100 nm in the as-received specimen to ~ 10–20 nm in both the cold and warm rolled and aged samples.

A bright diffusion field can be seen around the larger primary α grains in both the cold and warm rolled and aged samples, which is highlighted by the yellow lines in Fig. 1. It appears that the finer scale α has not grown from the α/β interface, which is observed in both the BSE-SEM and HAADF-STEM micrographs.

Transmission Kikuchi Diffraction (TKD) was used to identify the orientations of the secondary α that were present within the specimens. This was completed on the as-received and cold rolled and aged samples. Figure 1c, d shows the as-received orientation with the corresponding (0001) pole figure from a selection of secondary α grains, and Fig. 1g, h shows the orientations of the cold rolled and aged sample along with the (0001) pole figure. Due to the secondary α in Fig. 1g being significantly smaller, thermal drift in the microscope was a significant challenge, leading to more noise in the resultant data. This can also be seen in the difference in the pole figures in Fig. 1d, h, where there were fewer points to analyse due to more noise in the data caused by residual strain in the specimen from the cold rolling, causing distorted Kikuchi patterns. The circles in Fig. 1d, h highlight the 6 most

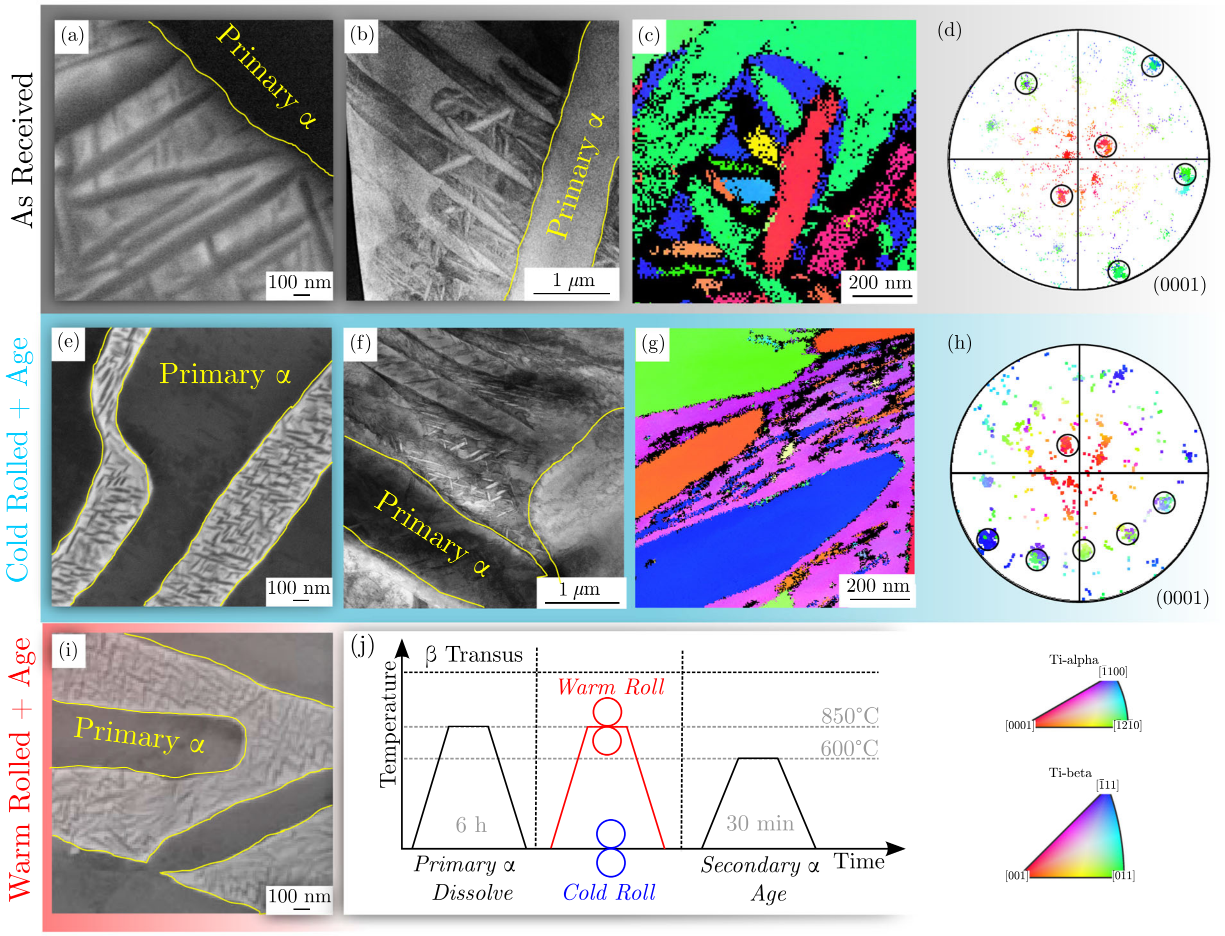

Fig. 1 | Microstructure of the as-received, warm rolled and aged, and cold rolled and aged specimens along with TKD maps and processing diagram. a–d as-received microstructure of Ti-6246 in Backscattered Electron Scanning Electron Microscopy(BSE-SEM), High Angle Annular Dark-Field Scanning Transmission Electron Microscopy (HAADF-STEM) and Transmission Kikuchi Diffraction with the corresponding (0001) pole figure with only secondary α_s grains selected for analysis. **e–h** shows the same for the 10% cold rolled and aged sample. Highlighted regions on the pole figures represent six orientations which each have 2 reflections, therefore showing 12 α_s variants. **i** Warm rolled and aged microstructure after 31% deformation in BSE. **j** Processing diagram for warm rolled and aged and cold rolled and aged processes. All work was done below the β transus.

common orientations, which can be further separated into 12 orientations. All 12 variants cannot be observed on a single pole figure, due to the Burgers orientation relationship, where the $[11\bar{2}0]$ α is parallel to the [111] β. The crystal symmetry results in 2 variants sharing the same {0002} pole direction. Therefore, to observe all 12 variants, they must be observed in both the $\{11\bar{2}0\}$ and the {0002} directions. These 12 variants are displayed in Fig. 2, labelled (a) to (l), where the 6 primary orientations are shown in the {0002} pole figure, highlighted by a diamond, and the double spot reflections are shown in the $\{11\bar{2}0\}$ pole figure, highlighted by a solid circle and a dotted circle for the 2 separate variants. These pole figures were taken from selected areas with only secondary alpha, showing that all possible 12 α variants of secondary α are present according to the Burgers orientation relationship. Therefore, the change in processing parameters has not instigated a change in the secondary α texture; only a grain size change.

In-situ TEM

In order to investigate secondary α growth, in situ ageing was performed simultaneously with High Angle Annular Diffraction-Scanning Transmission Electron Microscopy (HAADF-STEM) and 4D-Scanning Transmission Electron Microscopy (4D-STEM). The specimen had been heat treated at 850 °C to remove secondary α and cold rolled prior to a specimen being prepared for HAADF-STEM. Figure 3a, b shows the specimen prior to heating in situ. In Fig. 3a, dislocations can be seen within the β matrix as shown by yellow triangles which appear as dark grey lines. Bright Field Transmission Electron Microscopy (BF-TEM) was used to observe this area as diffraction contrast in this imaging mode highlights dislocations within the specimen caused by localised strain. Figure 3b shows the beginning of the in-situ heating experiment. There is a lack of secondary α within the specimen. When secondary α is present within the light grey β matrix observed in HAADF, small lenticular features are present, which are shown in Fig. 1b, f. HAADF-STEM is used to observe microstructural changes as it is dependent on the Z number of the specimen, and therefore will show elemental segregation. This is particular useful in Ti-6246 as Mo acts as a β stabiliser and will be rejected as the α phase forms, showing a distinct difference in contrast between the α and β phases. Figure 3c, d shows HAADF-STEM micrographs of a sample that was aged in-situ at 850 °C in-situ from 0 to 393 s. The TEM foil had previously been increased in temperature over 3 h 28 min in an attempt to find the temperature of nucleation, as explained in the methods section. There is a large primary α grain in view at the top of both images, with the β matrix appearing below. There are smaller secondary α lathes within the β matrix away from the α/β interface, each surrounded by a bright halo. As HAADF-STEM is largely dependent on the Z number of the material, it can be inferred that molybdenum is being rejected during the growth of the secondary α, which has been previously shown in Ti-6246[10]. However, it may also be due to other elements partitioning, or due to strain. Prior to heating (Fig. 3a, b, there was no secondary α present in the foil. There is a substantial size difference between the secondary α observed in Fig. 3c, d of ~ 40–90 nm, indicating a speed of growth of ~ 0.17 nm s^{-1}. Comparing this to the velocity of primary α growth observed in the literature, it is significantly slower[10], perhaps due to the lack of solutes available for growth, or due to the method of in-situ growth here, where the growth speed may be effected by thin foil effects. It therefore cannot be conclusively determined that secondary α nucleating and growing from dislocations grows at a slower velocity than standard nucleation from the α/β interface.

Figure 4 shows the resulting 4D-STEM data. These datasets were not collected at the same time as the HAADF-STEM images in Fig. 3 as the microscope was realigned in order to reduce the probe convergence semi-angle to 2.3 mrad. Nanobeam electron diffraction (NBED) patterns were collected in a 256 × 256 configuration and analysed using strain calculation and pattern matching algorithms described in previous literature[16–18]. Virtual dark field (VDF) images were formed from the diffraction patterns collected during 4D-STEM. The top and bottom of the strain maps show (0002) primary α grains. Strain in the v direction (ε_{vv}), which is aligned with the $[0002]_\alpha//[101]_\beta$ direction of the summed diffraction pattern, shown as the reference diffraction pattern in Fig. 4, shows a significant evolution of the microstructure. Fine scale secondary α has nucleated and grown in bands corresponding to the $\{101\}_\beta$ direction, corresponding to slip bands within the β matrix. In the (ε_{uu}) direction, fine α can be observed adjacent to the top primary α lamellae, corresponding to the $[0002]_\alpha$ direction. The strain within the β matrix decreased with increased time at temperature. It can therefore be assumed that as the fine scale α grows, there is lattice extension along the growth direction causing a contraction in the lattice perpendicular to this. The shear term, (ε_{uv}), increases significantly over time, as does the lattice rotation. The reference diffraction pattern, summed over all patterns for 0 s, and HAADF and VDF (virtual dark field) micrographs are also shown. The VDF images after heating show significantly more detail compared to HAADF, primarily revealing more nanoscale phases present. This is likely due to the VDF capturing more diffraction contrast due to the reduced angular range.

Mechanical testing

Results for hardness and tensile test for both the as-received and warm rolled and aged specimens are shown in Fig. 5. Large scale components cannot experience significant cold deformation, and therefore the warm rolling route was the focus of the mechanical investigations. When the secondary α is dissolved before rolling, there is a significant drop in hardness. After rolling and ageing, there is a ~ 10% increase in the hardness of both the cold and warm processed material. The as-received materials had a 0.2% tensile yield strength of 954 MPa with a ductility of 16%. The warm rolled and aged sample has a 0.2% yield strength of 1037 MPa with a ductility of 12%. This translates to a 8% increase in yield strength, with a slight loss in ductility.

Stress (S) - life (N) results for the fatigue tests are presented in Fig. 6a with an inset table showing results for High Cycle Fatigue (HCF) step testing to find peak stress. Although there is some deviation between samples (perhaps due to variation in the primary α), the trends can be analysed. The warm rolled and aged route has a 150 MPa improvement on the as-received material, around 15% in step testing. At longer lifetimes, there is an even larger distinction with a 200 MPa difference at lifetimes approaching 10^7 cycles.

Figure 6b shows the results from fatigue crack growth testing. The ΔK_{th} (stress intensity threshold) from the as-received Ti-6246 is 6 MPa$\sqrt{m}^{-1}$ whereas for the warm rolled and aged processing route it is 4 MPa$\sqrt{m}^{-1}$. However, the crack growth rate (da/dN, where a is the crack length and N is the number of cycles) for the edited route is slower than that of the as-received material. Therefore, though crack initiation may occur at a lower stress intensity in the fine α material, the crack will grow slower and fail at a similar ΔK to the as-received material.

Discussion

Secondary α morphology and growth

The impact of deformation on the size of the resulting secondary α phase is clearly evident in Fig. 1. By deforming the material dislocations are added, particularly in the β matrix. By adding dislocations into the β matrix, high energy nucleation sites are added, presenting an alternative nucleation point to the α/β interface. The 600 °C ageing step then supplies the additional activation energy *via* heat to encourage nucleation and growth of secondary α precipitates. As there are now multiple high energy points available within the β matrix by means of dislocations, it can be assumed that the secondary α lath size reduction is due to simultaneous nucleation and growth. Once the concentration of α stabilisers within the β matrix reaches a minimum, coarsening can no longer be achieved, resulting in a smaller secondary α lath size due to soft impingement.

Confirmation of the assumption that secondary α growth does not occur at the α/β interface is seen in Fig. 1; this will also be inhibited by the presumed Mo solute field around the primary α plates, which we have observed previously[10]. No secondary α is seen to grow from the α/β interface, with all nucleation occurring within the β matrix. As HAADF-STEM is

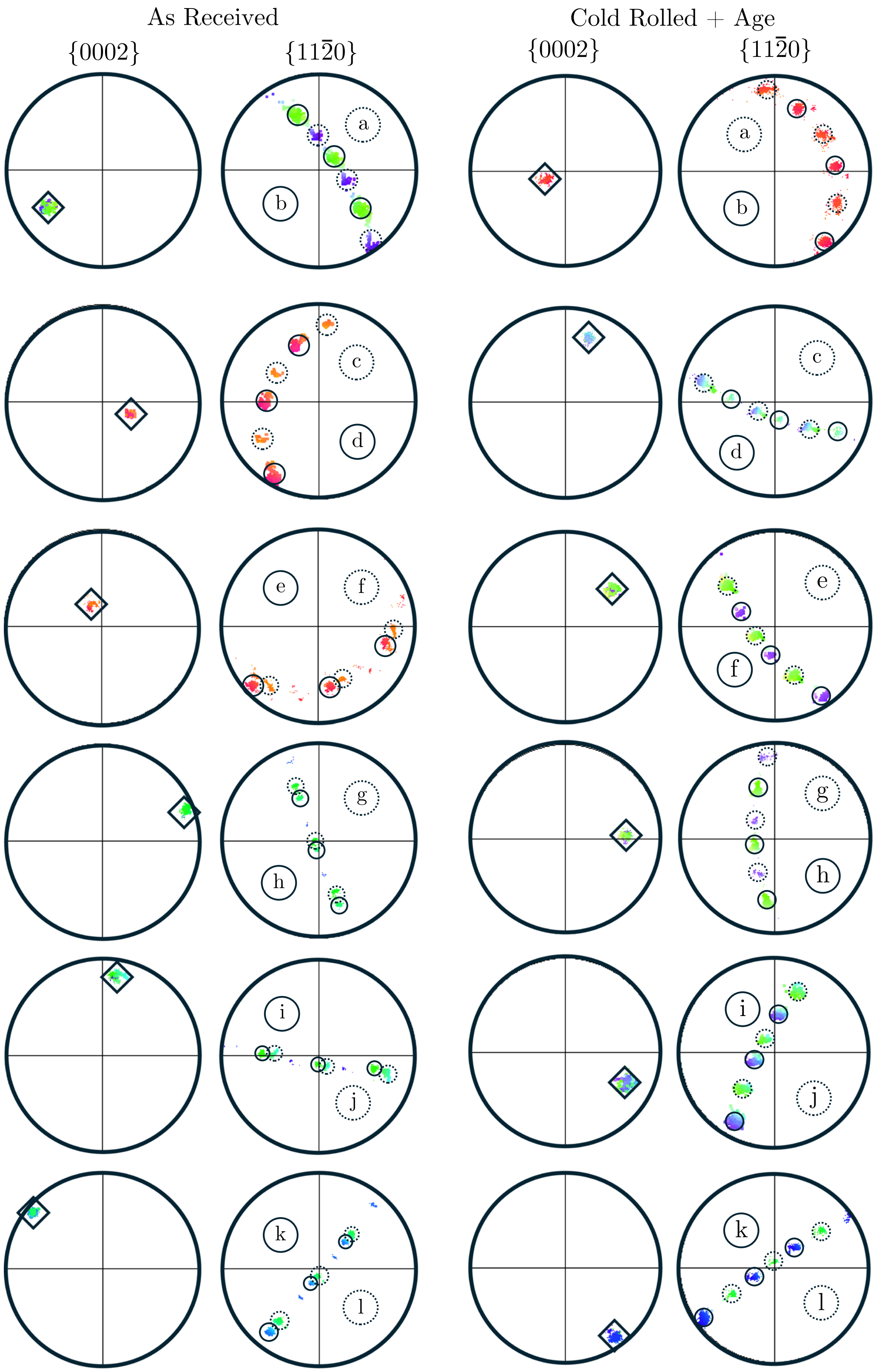

Fig. 2 | Pole figures of the alpha variants found in both the as received and the cold rolled and aged specimens, segmented by each distinct direction shown in the {0002} pole figures. The {0002} pole figures show 6 distinct variants highlighted by a diamond, and the corresponding {11$\bar{2}$0} pole figure shows each spot doubled, highlighted by the solid circles for the first of the variant pair, and a dotted circle for the second of the variant pair. This indicates that 12 distinct variants are present in both samples.

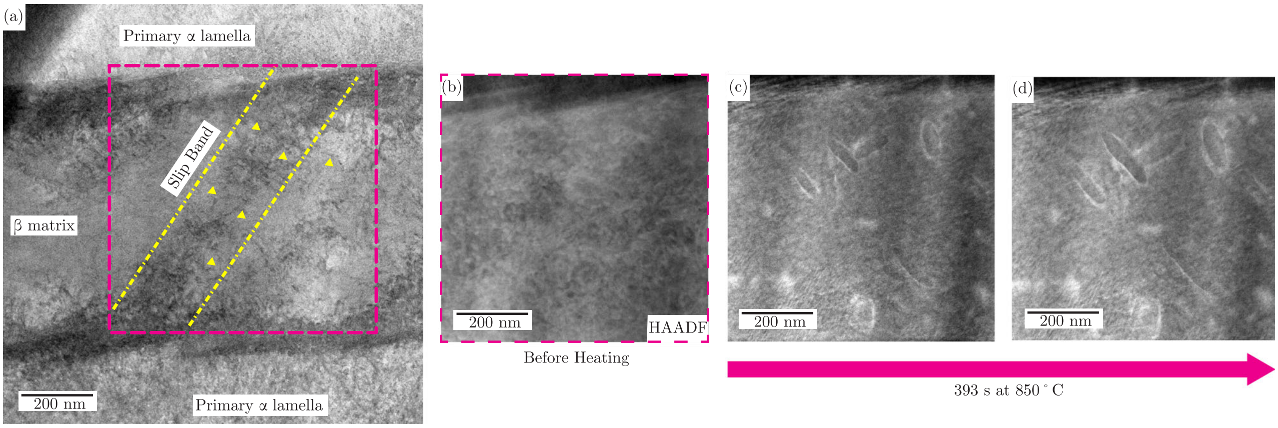

Fig. 3 | Transmission electron microscopy images of microstructures evolution in the cold rolled specimen. **a** Bright Field Transmission Electron Microscopy (BF-TEM) and **b** High Angle Annular Diffraction-Scanning Transmission Electron Microscopy (HAADF-STEM) micrographs of the same area, prior to heating. The yellow triangles show examples of dislocations. **c**, **d** HAADF-STEM micrograph of in situ ageing of secondary α within the β matrix, over a period of 393 s at a temperature of 850 °C.

highly dependent on the atomic number of the atoms, the bright white field that appears around the secondary α is assumed to be caused by the rejection of Mo as the α phase forms, though this may also be due to strain around forming secondary α phase as it forms. This phase was aged in situ at 850 °C, which is 250 °C higher than the ageing temperature used in conventional bulk testing. The higher temperature was necessary to compensate for thermal instability across the DENS chip and heat loss through the thin TEM foil, an issue previously reported by Hajraoui et al.[19]. As a result, a higher temperature was required to initiate secondary α growth in the TEM sample.

The evolution of strain at a temperature of 1050 °C is presented in Fig. 4. The temperature had to be increased to encourage the growth of secondary alpha. This is most likely due to thin film effects. The specimen has shown growth of α along $\{110\}$ bands. $\{110\}$ slip bands connecting large steps at the α/β interface have been previously observed after 10% cold rolling of Ti-6246[20]. This has additionally been observed by Furuhara et al.[21], where cold rolling Ti-Cr, a β titanium alloy, and subsequent ageing resulted in formation of fine α precipitates along the $\{112\}$ slip bands within the β matrix. The fine α plates observed near the α/β interface exhibit a morphology similar to that reported by Furuhara et al. and may share the same crystallographic orientation. Specifically, the [0002] direction in α is parallel to the [110] direction in β, which lies perpendicular to the $\{112\}$ planes, indicating that the plates are likely in-plane. In addition to this, there is a lattice extension along the fine secondary α growth direction, with a compression perpendicular to this. This may be attributed to an evolution of lattice parameters as the α phase is growing within the β matrix. Interestingly, there appears to be lattice rotation occurring with a high level of shear, Fig. 4. This again can most probably be attributed to the lattice parameters evolving as the α phase grows. This analysis gives insight into the strain evolution as α grows, and how the strain evolves to accommodate the strain field of the dislocation, which has been previously commented on in the literature[22].

Figure 1 compares the orientation of as-received disc material and cold rolled and aged samples with a secondary α size comparison to the warm rolled and aged process. The pole figures in Fig. 2 highlight 6 of the strongest orientations in the $\{0002\}$ along with the 2 reflection present in the $\{11\bar{2}0\}$, selected only from secondary α laths. This means that there is no loss of secondary α variants when there is nucleation from dislocations rather than the α/β interface, therefore the random basketweave texture is retained, and any change in mechanical test data will be primarily due to the size effect of the secondary α. Qui et al.[23] have shown that variant selection can occur via dislocations using phase field modelling. In this study, it has been shown that variant selection has not occurred, as all 12 variants are present. Though texture anisotropy has been seen due to deformation is previous studies, this is primarily of influence to the primary α microstructure[24]. In this case, as the secondary α is nucleating from dislocations within the β matrix rather than the interface, the effect is not substantial enough to cause texture anisotropy.

Mechanical test performance

Figure 5 shows that the finer microstructure from the edited processing route results in a higher yield strength, though the material is now less ductile. From the hardness values in the inset table, it can be seen that without the presence of any secondary α, there is a significant drop in hardness, and therefore strength. This indicates that the presence of finer secondary α is the basis for the increase in strength and not as a result of work hardening. Though it is possible that work hardening has occurred after deformation, the subsequent ageing step which initiates to nucleation and growth of secondary α will remove this effect by relieving the stored stress in the matrix. Additionally, the hardness values for the cold rolled and aged and the warm rolled and aged samples are comparable. Therefore, it can be assumed that despite the change in process temperature, it is possible to retain adequate dislocation content upon warm rolling to encourage the nucleation and growth of fine scale secondary α from defects within the β matrix.

The additional mechanical testing results in Fig. 6 shows that the warm rolled and aged alternative processing route with finer secondary α retains its fatigue strength at higher cycles, more so that the standard processing route. In fact, there is only a drop of 100 MPa, compared to the as-received material which has a drop of 250 MPa. Such retention of strength at high cycles means that a manufactured engine part could be used for a longer period of time, reducing costs and improving efficiency. In Fig. 6b, the crack growth threshold (ΔK_{th}) and crack growth rate can provide some explanation for this. Though the edited route has a slightly lower crack threshold value, the crack growth rate is much slower than the as-received Ti-6246. As detailed earlier, there is no significant change in texture provided by defect stimulated α growth, therefore it can be assumed that it is the change in effective slip length that has caused the improvement in mechanical properties.

The present material achieves exceptional cyclic fatigue strength due to its ability to form fine-scale α within grains, nucleated from nanoscale defects, similar to the behaviour observed in near-β titanium alloys such as Ti-10-2–3. In comparison testing (Fig. 6), it demonstrates a fatigue strength advantage of 150 MPa at 10^6 cycles for an un-notched plain bar. This performance matches that of landing gear alloys, but in a material designed for high-temperature applications, as summarised in Table 1. These results are in good agreement with prior work completed by Lütjering[25,26], where it was

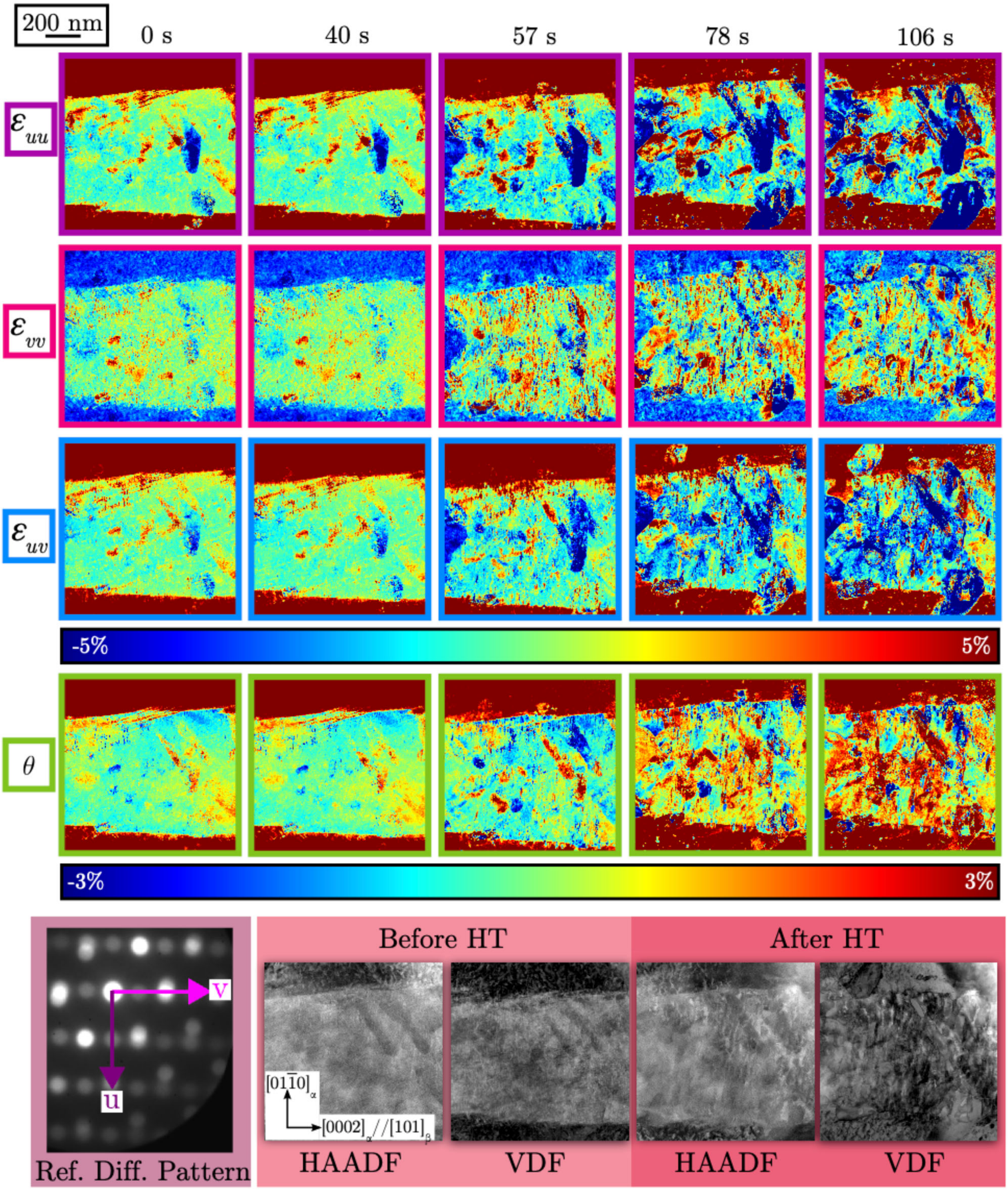

Fig. 4 | 4D-STEM strain maps taken from 0 to 106 s at a temperature of 1050 °C. The foil had previously been heated to 850 °C and taken back to room temperature. The beam direction used was $[111]_\beta//[11\bar{2}0]_\alpha$. The **u** direction corresponds to the $[01\bar{1}0]_\alpha$ and the **v** to $[0002]_\alpha//[101]_\beta$, as shown in the inset diffraction pattern. All directions are with respect to the primary α, which was fabricated to be on the basal plane. ε_{uu}, ε_{vv} and ε_{uv} range from −5 to 5% strain, and the lattice rotation θ ranges from −3 to 3%.

observed that smaller colony sizes impact the slip length, resulting in higher strength, HCF and LCF.

Conclusions

A change in the thermomechanical processing of aerospace alloy Ti-6246 by either cold or warm rolling to introduce dislocations into the β matrix has been presented and investigated using high resolution characterisation techniques, mechanical testing and 4D-STEM. It has shown that:

1. Nucleation of a finer secondary α phase occurs from dislocations introduced *via* this new processing route.

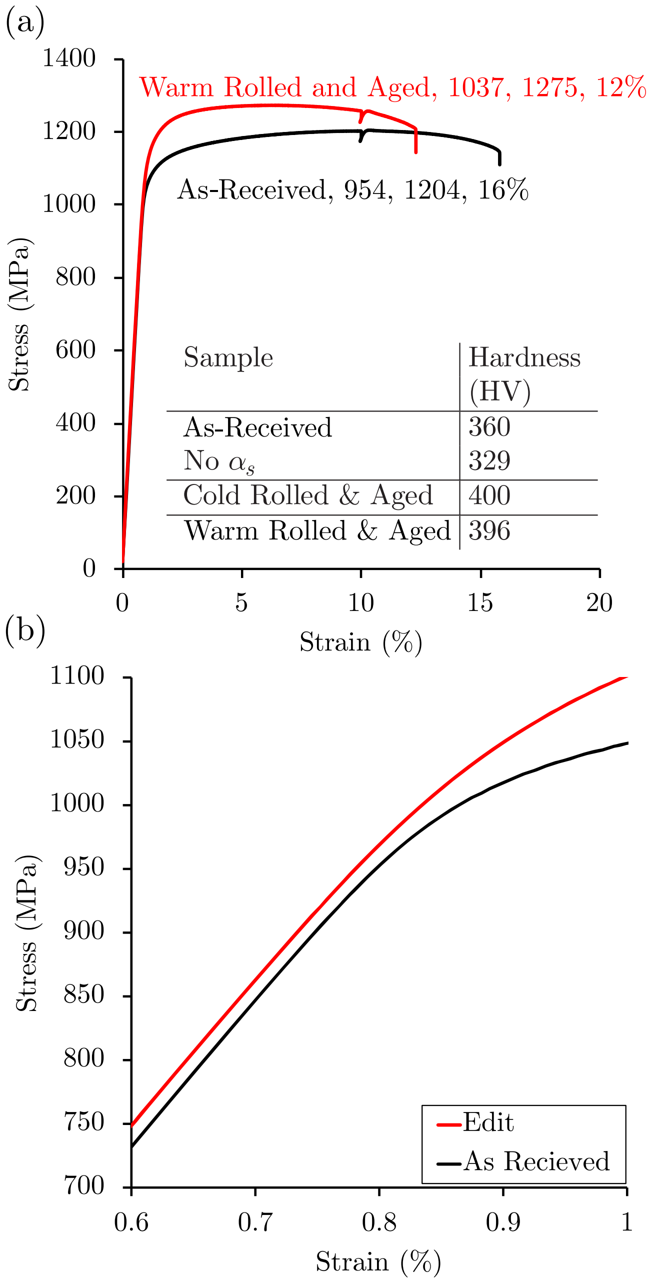

Fig. 5 | Tensile mechanical testing data comparing as-received material to warm rolled and aged. a Tensile curves of as-received Ti-6246 in black and material from the edited processing route in red, with corresponding 0.2% yield (MPa), ultimate tensile strength (MPa) and ductility values. The inset table shows hardness testing results for as received, material without primary α, after cold rolling and ageing, and after warm rolling and ageing. **b** An enlarged view of (**a**) to show the 0.2% yield strength difference in the as-received and edited route.

2. The multi-variant texture of secondary α is preserved when nucleation from dislocations occurs.
3. The process can be achieved at warm temperatures, allowing for use in scaled up metallographic processes.
4. Nucleation occurs along the {110} slip bands, and large rotation and shear strain is observed as the new phase grows into the existing lattice.
5. The finer secondary α microstructure provides an increase in yield strength of 8%, an increase of 15% peak HCF stress, and a slower crack growth rate.

Therefore, defect-stimulated nucleation can be used to provide finer length-scale microstructures, which have consequent improvements in performance. This strategy will be broadly usable in all titanium alloys that contain a secondary α phase with a slow enough diffusion rate to allow nucleation from defects, potentially changing the way we process titanium alloys in industry. This is significant in terms of jet engine materials. Such improvement could result in much smaller engine parts, leading to less weight and an increase in efficiency.

Methods

Samples were prepared from a forging of nominal composition Ti-6Al-2Sn-4Zr-6Mo (wt%) supplied by Rolls-Royce plc. Derby and therefore meet aerospace rotor grade specifications, which is nominally a maximum of 0.15 wt% O, 0.15 wt% Fe, 0.04 wt% N, 0.04 wt% C and 0.125 wt% H. The as-received material experiences deformation above the β transus and in the $\alpha+\beta$, followed by a controlled cooling at room temperature. The as-received material is then aged at 600 °C for 4 h followed by an air cool. Material for rolling was then heated to 850 °C in a vacuum furnace for 6 h, followed by a water quench. All specimens were loaded when the furnace has reached the appropriate temperature, to negate any heating rate effects. After rolling, the specimens were then aged at 600 °C for 30 min in air, followed by an air cool.

Physical and microstructural characterisation

Electron Backscatter Diffraction (EBSD) and backscatter electron scanning electron microscopy (BSE-SEM) was performed using a Zeiss Sigma300 FEG-SEM fitted with an Oxford Instruments EBSD detector to locate a $(0002)_\alpha//\{110\}_\beta$ grain for TEM lift out. TEM samples for both in situ TEM and TKD were prepared using an FEI Helios NanoLab 600 DualBeam system equipped with an Omniprobe^{TM}. TKD maps were obtained on a Zeiss Merlin equipped with a Bruker on-axis e-flash HD detector. HAADF-STEM and 4D-STEM was completed using a JEOL Grand ARM300F in combination with a DENS Wildfire double tilt holder. Diffraction patterns for 4D-STEM were collected using a Medipix-3 direct electron detector using Merlin software. An accelerating voltage of 200 kV and a camera length of 9 cm was used, with a 10 μm condenser lens aperture. In order to collect data for 4D-STEM, a pencil beam condition was achieved by switching off the probe corrector hexapoles and using the condenser and transfer lens pairs to create a small convergence semi angle of 2.3 mrad, with a 1.3 ms dwell time used for exposure time per probe position. The 4D-STEM data was collected in a 256 × 256 configuration. Initially the DENS in-situ heating chip was heated in 50 °C until nucleation was observed at 850 °C. Heating was near instantaneous due to the nanoscale surface area of the foil. After collection of HAADF-STEM data, the sample was cooled instantly to room temperature as the microscope was realigned for 4D-STEM. The sample was then reheated to 850 °C and again heated in 50 °C until growth of the secondary α was observed at 1050 °C. As explained in the discussion, it is known in the literature that thin film effects can impact nucleation and growth in TEM foils, which explains the change in ageing temperature.

Tensile tests were completed using a 30 kN Instron tensile tester with an extensometer at a strain rate of 10^{-3} s^{-1}. HCF testing was completed using an Amsler Vibrophone at a frequency of 85 Hz and stress ratio $R = 0.1$. LCF and corner crack testing was completed using a 100kN Mayes with an Instron controller. A Matelect DCPD unit was used to apply a potential of 5 V and measure the potential drop as the crack grew. All tensile, HCF and LCF test specimens were machined to a specimen size with M11 thread and a 5mm gauge diameter. Fatigue crack growth test specimens were machined to an M12 thread with a 5 mm square cross section with a crack depth 0.25 mm.

Diffraction patterns were analysed using strain calculation and pattern matching algorithms described in previous literature[16–18]. For this study, the beam direction used was $[111]_\beta//[11\bar{2}0]_\alpha$. For directional strain analysis in Fig. 4, the **u** direction corresponds to the $[01\bar{1}0]_\alpha$ and the **v** to $[0002]_\alpha//[101]_\beta$ with respect to the primary α phase.

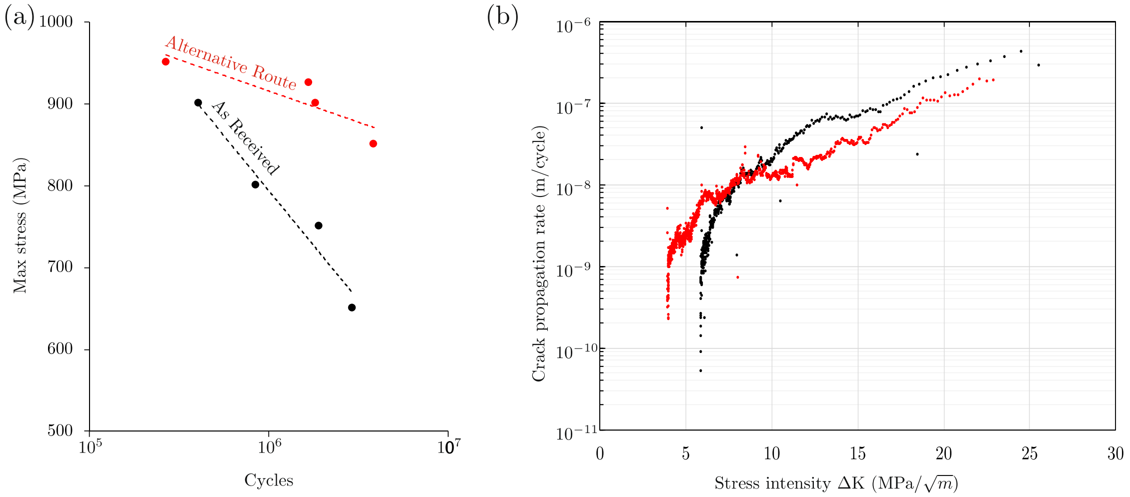

Fig. 6 | Mechanical testing data comparing as-received material to warm rolled and aged. a Graph of maximum stress against lifetime, tested in plane HCF at $R = 0.1$, and **b** fatigue crack growth rate against stress intensity ΔK. Results of the as-received Ti-6246 material are shown in black, whilst the material from the warm rolled and aged processing route in shown in red.

Table 1 | Comparison of the usable strength of mechanical properties of the present material to other high strength materials

Material	ρ gcm^{-3}	σ_{UTS} MPa	σ_y MPa	ε_f %	σ_{HCF} MPa	σ_{HCF}/ρ Jkg^{-1}
Ti 6246[27]	4.64	1242	1152	14	750	161
Ti 10-2-3[28]	4.65	1214	1145	12	910	195
This paper	4.64	1275	1037	12	950	204
300M steel[29]	7.84	1930	1700	-	1100	140

Landing gear alloys such as 300M steel and Ti 10-2-3 are shown for comparison.

Data availability

The data that support the findings of this study are available from the corresponding author upon reasonable request, a.ackerman14@imperial.ac.uk.

Code availability

Code used for data analysis of the 4D-STEM data can be accessed via GitHub at cophus/py4DSTEM.

Received: 7 July 2025; Accepted: 28 January 2026;
Published online: 17 March 2026

References

1. Banerjee, D. & Williams, J. C. Perspectives on titanium science and technology. *Acta Mate.* **61**, 844–879 (2013).
2. Lütjering, G. & Williams, J. C. *Titanium*, Springer (2003).
3. Kroll, W. The production of ductile titanium. *Trans. Electrochem. Soc.* **78**, 35 (1940).
4. Seagle, S., Yu, K. & Giangiordano, S. Considerations in processing titanium. *Mater. Sci. Eng. A* **263**, 237–242 (1999).
5. Semiatin, S., Knisley, S., Fagin, P., Zhang, F. & Barker, D. Microstructure evolution during alpha-beta heat treatment of Ti-6Al-4V. *Metall. Mater. Trans. A* **34A**, 2003–2017 (2000).
6. Kherrouba, N., Bouabdallah, M., Badji, R., Carron, D. & Amir, M. Beta to alpha transformation kinetics and microstructure of Ti-6Al-4V alloy during continuous cooling. *Mater. Chem. Phys.* **181**, 462–469 (2016).
7. van Bohemen, S., Kamp, A., Petrov, R., Kestens, L. & Sietsma, J. Nucleation and variant selection of secondary α plates in a β Ti alloy. *Acta Mater.* **56**, 5907–5914 (2008).
8. Sauer, C. & Lütjering, G. Influence of α layers at β grain boundaries on mechanical properties of Ti-alloys. *Mater. Sci. Eng. A* **319-321**, 393–397 (2001).
9. Peters, J. O., Lütjering, G., Nalla, R. K., Altenberger, I. & Ritchie, R. O. High cycle fatigue of beta-titanium alloys. *Fatigue 2002 Stockholm* **6246** http://www.lbl.gov/Ritchie/Library/poster/1_Fatigue2002-HCFofBetaTitaniumAlloys.pdf (2002).
10. Ackerman, A. K. et al. The kinetics of primary alpha plate growth in titanium alloys. *Metall. Mater. Trans. A: Phys. Metall. Mater. Sci.* **51**, 131–141 (2020).
11. Wang, K. & Li, M. Morphology and crystallographic orientation of the secondary α phase in a compressed α/β titanium alloy. *Scr. Mater.* **68**, 964–967 (2013).
12. Shi, R., Dixit, V., Fraser, H. & Wang, Y. Variant selection of grain boundary α by special prior β grain boundaries in titanium alloys. *Acta Materialia* **75**, 156–166 (2014).
13. Clément, N. *Phase transformations and mechanical properties of the Ti-5553 beta metastable titanium alloy*. Ph.D. thesis, Université catholique de Louvin (2010).
14. Lenain, A., Clément, N., Véron, M. & Jacques, P. J. Characterization of the α phase nucleation in a two-phase metastable β titanium alloy. *J. Mater. Eng. Perform.* **14**, 722–727 (2005).
15. Nyakana, S. L., Fanning, J. C. & Boyer, R. R. Quick reference guide for β titanium alloys in the 00s. *J. Mater. Eng. Perform.* **14**, 799–811 (2005).
16. Pekin, T. C., Gammer, C., Ciston, J., Minor, A. M. & Ophus, C. Optimizing disk registration algorithms for nanobeam electron diffraction strain mapping. *Ultramicroscopy* **176**, 170–176 (2017).
17. Ozdol, V. B. et al. Strain mapping at nanometer resolution using advanced nano-beam electron diffraction. *Appl. Phys. Lett.,* **106**, 253107 (2015).
18. Béché, A., Rouvière, J. L., Barnes, J. P. & Cooper, D. Strain measurement at the nanoscale: comparison between convergent beam electron diffraction, nano-beam electron diffraction, high resolution imaging and dark field electron holography. *Ultramicroscopy* **131**, 10–23 (2013).
19. Hajraoui, K. E. In-situ transmission electron microscopy studies of metal-Ge nanowire solid-state reactions. Ph.D. thesis, Université Grenoble Alpes (2017).
20. Ackerman, A. K. et al. Interface characteristics in an α+β titanium alloy. *Phys. Rev. Mater.* **4**, 1–7 (2020).
21. Furuhara, T., Nakamori, H. & Maki, T. Crystallography of α phase precipitated on dislocations and deformation twin boundaries in a β

titanium alloy http://www.jim.or.jp/journal/e/pdf3/33/06/585.pdf (1992).
22. Luo, C. P. & Weatherly, G. C. The crystallography of heterogeneous nucleation in a Ni-45 wt% Cr alloy. *Acta Metall.* **37**, 791–801 (1989).
23. Qiu, D., Shi, R., Zhang, D., Lu, W. & Wang, Y. Variant selection by dislocations during α precipitation in α/β titanium alloys. *Acta Mater.* **88**, 218–231 (2015).
24. Weiss, I., Froes, F. H., Eylon, D. & Welsch, G. E. Modification of alpha morphology in Ti-6Al-4V by thermomechanical processing. *Metall. Trans. A* **17**, 1935–1947 (1986).
25. Peters, J. O. & Lütjering, G. Comparison of the Fatigue and Fracture of a1 band b Titanium Alloys. *Metall. Mater. Trans. A* **32**, 2805–2818 (2001).
26. Lütjering, G. Influence of processing on microstructure and mechanical properties of alpha + beta titanium alloys. *Mater. Sci. Eng. A* **243**, 32–45 (1998).
27. Timet Metals Corporation, TIMETAL 6-2-4-6 Data Sheet, TMC-0151, Available: https://www.timet.com/documents/datasheets/alpha-and-beta-alloys/timetal-6246.pdf (2000).
28. Timet Metals Corporation, TIMETAL 10-2-3 Data Sheet, TMC-0000, Available: https://www.timet.com/documents/datasheets/metastable-beta-alloys/timetal-10-2-3.pdf (2000).
29. Latrobe Specialty Steel Company, LESCALLOY® 300M VAC-ARC® Data Sheet, Available: https://www.carpentertechnology.com/hubfs/7407324/Material%20Saftey%20Data%20Sheets/30M.pdf (2007).

Acknowledgements

The authors acknowledge funding from EPSRC (grant EP/K034332/1), Rolls-Royce plc and Imperial College. The assistance of Dr. Alexander Knowles in discussions surrounding the focused ion preparation process is greatly appreciated. We are grateful to the Electron Physical Sciences Imaging Centre (ePSIC) and Diamond Light Source for access to E02, proposal number EM18190. Work at the Molecular Foundry was supported by the Office of Science, Office of Basic Energy Sciences, of the U.S. Department of Energy under Contract No. DE-AC02-05CH11231. The authors acknowledge use of characterisation facilities within the David Cockayne Centre for Electron Microscopy, Department of Materials, University of Oxford, alongside financial support provided by the Henry Royce Institute (Grant ref EP/R010145/1).

Author contributions

A.K.A. and D.D. designed the study. A.A. completed thermomechanical testing, mechanical testing and data analysis, as well as SEM. B.S. and C.O. analysed the 4D-STEM data. M.D. performed TEM experiments. P.K. performed TKD experiments whilst A.K.A. analysed the resultant data.

Competing interests

The authors declare no competing interests.

Additional information

Supplementary information The online version contains supplementary material available at https://doi.org/10.1038/s43246-026-01096-y.

Correspondence and requests for materials should be addressed to Abigail K. Ackerman.

Peer review information *Communications Materials* thanks the anonymous reviewers for their contribution to the peer review of this work. A peer review file is available.